

# Comparison of the Dynamic Thin Shell and Quasi-cylindrical Models for Blown Film Extrusion

J. CARL PIRKLE, JR. and RICHARD D. BRAATZ

600 South Mathews Avenue, Box C-3  
University of Illinois at Urbana-Champaign  
Urbana, IL 61801

Most models of blown film extrusion are based on thin shell theory, which was first applied to these processes by Pearson and Petrie. There has been some contention in the literature as to the suitability of the thin shell model. More recently, Liu and co-workers presented an alternative quasi-cylindrical model that neglects longitudinal curvature but was reported to agree more closely with experiments. In later studies, other researchers used the quasi-cylindrical model to investigate flow-induced crystallization. The current paper presents finite difference solutions of the quasi-cylindrical model and quantifies the differences in the steady-state behavior, dynamics, and stability between the quasi-cylindrical and the thin shell models. The differences in the steady-state and dynamic behavior between the thin shell and quasi-cylindrical models are found to be significant, both qualitatively and quantitatively. This study should aid future researchers in developing dynamic simulation models that include more sophisticated descriptions of the underlying polymer physics.

Polym. Eng. Sci. 44:1267–1276, 2004. © 2004 Society of Plastics Engineers.

## INTRODUCTION

The thin shell model is the most heavily studied steady-state description for blown film extrusion (1, 2) (see Fig. 1). During an extensive experimental and modeling effort, Liu and co-workers (3–5) reported that the thin shell model did not agree qualitatively with experimental results. According to their calculations, for a constant take-up ratio ( $TUR = V_L/V_0$ ) the thin shell model appeared to predict a decrease in blow-up ratio ( $BUR = R_L/R_0$ ) with an increase in bubble inflation pressure, which was counter to their experimental observations. There were other disagreements between the computational and experimental results as well, such as the effect of extrusion temperature on bubble dimensions. Because of these disagreements, Liu and co-workers proposed the quasi-cylindrical model (3) for blown film extrusion, which ignores longitudinal curvature of the bubble radius in the axial direction. Liu and co-workers reported that this simplification allowed them to obtain reasonable qualitative comparison

between experimental and model results. The quasi-cylindrical model was used by other researchers in later studies (6).

In recent work (7), steady-state solutions to the thin shell model were obtained by running transient finite difference calculations for sufficiently long time. These results disagreed qualitatively with the computational observations of Liu and co-workers, but were in accord with their experimental results (8). We suspect that the differences between computational results of (7) and (3–5) are due to the methods of calculation. Liu and co-workers solved the system of ordinary differential equations constituting the steady-state thin shell model as an initial value problem, even though the initial value of one of the variables (the slope of the bubble radius) is not known (it was assumed to be zero, as done by Ashok and Campbell (9)). Our numerical method did not presuppose knowledge of this condition. Further, it was shown that past boundary conditions downstream of the frost line used by numerous researchers to simulate blown film extrusion give physically unrealistic steady-state behavior (see Ref. 7) for details, including references to other simulation papers). Thus, a boundary condition was proposed that produces results that are consistent and physically meaningful.

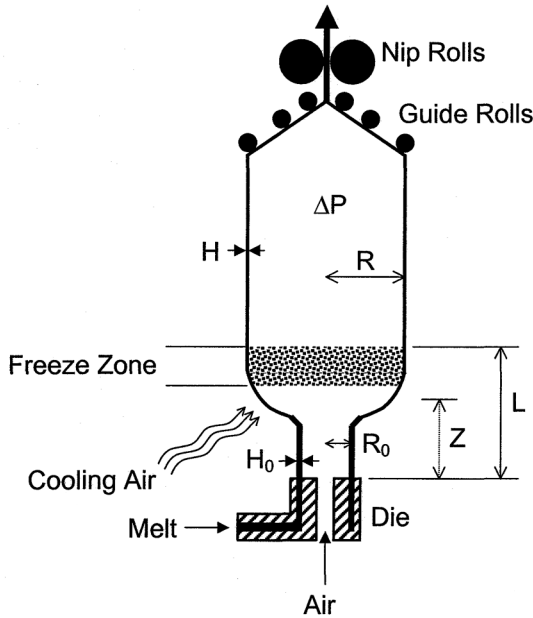


Fig. 1. Schematic of blown film extrusion.

In this paper, we present finite difference solutions of the quasi-cylindrical model and quantify the differences in the steady-state behavior, dynamics, and stability between the quasi-cylindrical and the thin shell model when both models use the same physical parameters and constitutive equation (7). The main goal of this study is to make a definitive recommendation as to the suitability of the quasi-cylindrical model for simulating blown film extrusion, for either steady-state or dynamic studies.

**DYNAMIC VERSION OF THE QUASI-CYLINDRICAL MODEL**

The thin shell model using the same constitutive equation and physical parameters is described in a previous paper (7), so only the quasi-cylindrical model is described here. The quasi-cylindrical model (3) neglects longitudinal curvature in the continuity and both momentum equations of the thin shell model (1, 2) as well as the term  $B(r_f^2 - r^2)$  in the axial momentum equation. Using the dynamic form of the deformation rate tensor derived by Yeow (10), the dynamic model equivalent to the steady-state quasi-cylindrical model was derived. The continuity equation in the dynamic version of the quasi-cylindrical model is

$$h \frac{\partial r}{\partial \tau} + r \frac{\partial h}{\partial \tau} + rh \frac{\partial v}{\partial s} + rv \frac{\partial h}{\partial s} + hw \frac{\partial r}{\partial s} = 0 \quad (1)$$

where all variables and constants are defined in Table 1.

The momentum equation in the axial direction is

$$r \frac{\partial h}{\partial \tau} - rh \frac{\partial v}{\partial s} + rv \frac{\partial h}{\partial s} + hw \frac{\partial r}{\partial s} = -\frac{F}{2\eta} \quad (2)$$

Table 1. Symbols for Variables and Constants: Dimensional.

$b$	Exponent for denominator term of viscosity factor
$C_{pf}$	Specific heat of polymer
$C_3$	Coefficient in crystallization rate expression
$H_0$	Film thickness as it exits die at $Z = 0$
$H$	Film thickness at axial position $Z$
$H_L$	Film thickness at top boundary of freeze zone
$k_{crys}$	Crystallization rate coefficient
$L$	Axial position corresponding to top boundary of freeze zone
$N_Z$	Number of grid points in discretization of axial coordinate
$R$	Radius of film tube at axial position $Z$
$R_L$	Final radius of film tube at top boundary of freeze zone
$R_0$	Radius of film tube as it exits die at $Z = 0$
$t$	Time
$T$	Temperature of film tube at position $Z$
$T_{air}$	Temperature of cooling air
$T_\infty$	Equal to $T_g - 30K$ , where $T_g$ is the polymer glass transition temperature
$T_m$	Melt temperature of polymer
$T_0$	Temperature of film tube as it exits die at $Z = 0$
$U^*$	Activation energy for segmental jump rate in polymers
$V$	Velocity of film at axial position $Z$
$V_L$	Velocity of film at top boundary of freeze zone
$V_0$	Velocity of film as it exits die at $Z = 0$
$Z$	Axial position measured upward from position of die
$\alpha_1$	Adjustment coefficient for viscosity factor
$\alpha_2$	Adjustment coefficient for crystallization term in viscosity factor
$\beta_1$	Adjustment coefficient for temperature dependence of viscosity factor
$\beta_2$	Exponent for crystallization dependence of viscosity factor
$X$	Local fraction of crystallinity
$X_f$	Final crystallinity
$\Delta H_{crys}$	Heat of crystallization
$\Delta P$	Inflation pressure, relative to ambient pressure
$\lambda_a$	Relaxation time for stress thinning
$\Pi_d$	Second invariant of the deformation rate tensor
$\rho$	Polymer density
$R$	Universal gas constant
$\mu$	Viscosity of polymer
$\mu_0$	Viscosity of polymer as it exits die

and the momentum equation in the circumferential direction is

$$h \frac{\partial r}{\partial \tau} - r \frac{\partial h}{\partial \tau} - rv \frac{\partial h}{\partial s} + hw \frac{\partial r}{\partial s} = \frac{Br^2}{\eta} \quad (3)$$

The parameters  $B$  and  $F$  are defined in Table 2.

Unlike the thin shell model, no dependent variable is necessary to represent the longitudinal gradient of the bubble radius, as terms involving  $\partial^2 r / \partial s^2$  are ignored in the model.

The energy and crystallization equations are the same as in the thin shell model:

$$\frac{\partial \theta}{\partial \tau} + v \frac{\partial \theta}{\partial s} + B_2 \frac{(\theta - \theta_{air})}{h} - B_3 B_4 F_\theta (1 - x) = 0 \quad (4)$$

and

$$\frac{\partial x}{\partial \tau} + v \frac{\partial x}{\partial s} - B_4 F_\theta (1 - x) = 0 \quad (5)$$

**Table 2. Symbols for Variables and Constants: Dimensionless**

$B$	Dimensionless pressure force = $\Delta P R_0^2 / [2 \mu_0 H_0 V_0]$
$BUR$	Blow-up ratio = $R_L / R_0 = r_L$
$F$	Dimensionless elongational or machine tension
$h$	Dimensionless film thickness = $H / H_0$
$r$	Dimensionless film tube radius = $R / R_0$
$r_L$	Dimensionless film tube radius at top boundary of freeze zone = $BUR$
$TR$	Thickness reduction = $H_0 / H_L = 1 / h_L$
$TUR$	Take-up ratio = $v_L = V_L / V_0$
$v$	Dimensionless film velocity = $V / V_0$
$y$	Dimensionless derivative if radius with respect to axial position = $\partial r / \partial s$
$\chi$	Dimensionless crystallinity = $\chi = X / X_f$
$s$	Dimensionless axial position = $Z / R_0$
$\eta$	Dimensionless viscosity factor = $\mu / \mu_0$
$\theta$	Dimensionless temperature = $T / T_0$
$\theta_{air}$	Dimensionless temperature of air = $T_{air} / T_0$
$\nu$	Dimensionless frequency
$\tau$	Dimensionless time = $t V_0 / R_0$
$\Psi$	Dimensionless curvature function

where

$$B_2 = \frac{U_h R_0}{\rho C_{pf} H_0 V_0} \quad (6)$$

$$B_3 = \frac{\Delta H_{crys} X_f}{C_{pf} T_0} \quad (7)$$

$$B_4 = \frac{R_0 k_{crys}}{V_0} \quad (8)$$

In Eq 4, the heat loss term has the effect of radiation losses lumped into it by use of a larger value for the convective heat transfer coefficient  $U_h$ . This is a reasonable approximation since the heat loss by radiation is much smaller than the loss by convection.

In the above equations, the function  $F_\theta$  is the temperature-dependent factor for the rate of crystallization and is given by

$$F_\theta = 0 \quad \text{for} \quad \theta \geq \theta_m \quad (9)$$

$$F_\theta = \exp \left[ -\frac{B_{F1}}{(\theta - \theta_c)} - \frac{B_{F2}}{\theta(\theta_m - \theta)} \right] \quad \text{for } u, \text{ um} \quad (10)$$

The dimensionless constants  $B_{F1}$ ,  $B_{F2}$ ,  $\theta_m$ , and  $\theta_c$  are defined by

$$B_{F1} = \frac{U^*}{\Re T_0} \quad (11)$$

$$B_{F2} = \frac{C_3}{T_0^2} \quad (12)$$

$$\theta_m = \frac{T_m}{T_0} \quad (13)$$

$$\theta_c = \frac{T_\infty}{T_0} \quad (14)$$

As done in almost all models of blown-film extrusion (e.g., see papers cited in Ref. 7), flow-induced crystallization is ignored, although the validity of doing so is uncertain.

Note that Eqs 2, 4, and 5 are already decoupled with respect to the time derivatives of the variables. Rearranging Eqs 1, 2, and 3 gives the equations

$$h \frac{\partial r}{\partial \tau} + \frac{1}{2} r h \frac{\partial v}{\partial s} + h v \frac{\partial r}{\partial s} = \frac{B r^2}{2 \eta} \quad (15)$$

$$-\frac{3}{2} r h \frac{\partial v}{\partial s} + h v \frac{\partial r}{\partial s} = \frac{1}{2} \left( \frac{B r^2}{\eta} - \frac{F}{\eta} \right) \quad (16)$$

The boundary conditions in the dynamic quasi-cylindrical model are all located at the die exit:

$$r = 1 \quad \text{at} \quad s = 0 \quad (17)$$

$$h = 1 \quad \text{at} \quad s = 0 \quad (18)$$

$$v = 1 \quad \text{at} \quad s = 0 \quad (19)$$

$$\theta = 1 \quad \text{at} \quad s = 0 \quad (20)$$

$$x = 0 \quad \text{at} \quad s = 0 \quad (21)$$

### CONSTITUTIVE RELATION

While many constitutive relations have been used to describe the viscous properties of the polymer during its extrusion, the one used here is same constitutive relationship used by Liu and co-workers (3) and Pirkle and Braatz (7). Thus, the results can be directly compared. This constitutive relation takes into account stress thinning, temperature change, and crystallization. The viscosity of the film is expressed as

$$\mu = \mu_0 \eta \quad (22)$$

where the bases viscosity  $\mu_0$  is

$$\mu_0 = \alpha_1 \exp \left( \frac{\beta_1}{T_0} \right) \quad (23)$$

The dimensionless viscosity factor  $\eta$ , which accounts for temperature change and crystallization, is

$$\eta = \frac{\alpha_1 \exp \left( \frac{\beta_1}{T_0} \right) \exp(\alpha_2 \chi^{\beta_2})}{\mu_0 [1 + (\lambda_a \sqrt{\Pi_d})^b]} \quad (24)$$

Here,  $\alpha_1$ ,  $\alpha_2$ ,  $\beta_1$ ,  $\beta_2$ , and  $b$  are measured or adjusted constants, and  $\Pi_d$  and  $\lambda_a$  are the second invariant of the deformation rate tensor and the relaxation time, respectively. The denominator in Eq 24 provides for stress thinning. In terms of the dependent variables, the expression for  $\Pi_d$  is

$$\Pi_d = 2 \left( \frac{V_0}{R_0} \right)^2 \left[ \left( \frac{1}{r} \frac{\partial r}{\partial s} \right)^2 + \left( \frac{1}{h} \frac{\partial h}{\partial s} \right)^2 + \left( \frac{1}{r} \frac{\partial r}{\partial s} \right) \left( \frac{1}{h} \frac{\partial h}{\partial s} \right) \right] v^2 \quad (25)$$

## NUMERICAL METHOD OF SOLUTION

This paper uses the numerical method of lines (NMOL) (11) to solve the above system of partial differential equations (PDEs). This entails discretizing the equations in the spatial variable  $\varsigma$  at a number of grid points  $N_z$ . Spatial derivatives such as  $\partial v/\partial \varsigma$  are replaced by five-point finite differences in order to achieve 4th-order accuracy, thus eliminating the spatial variable as an independent variable. A variable-grid spacing technique that allows a choice of such 5-point finite differences is coded in the subroutine DSS032 (12). The discretization converts Eqs 2, 4, 5, and 15 to a set of  $4(N_z - 1)$  coupled ordinary differential equations (ODEs) containing time derivatives for the local (at each grid point) values of  $r$ ,  $h$ ,  $\theta$  and  $x$ . Equation 16 is converted into  $(N_z - 1)$  algebraic equations for the local values of  $r$ ,  $h$ , and  $v$ . Also, the boundary conditions (Eqs 17 to 21) are included in the system of ordinary differential and algebraic equations (DAEs) as five algebraic equations.

The resulting set of DAEs is solved using DASSL (13). All computations were performed in double-precision Fortran 77 using a Windows NT workstation with a 900 MHz Athlon processor. In coding the dynamic equations, the first grid point was selected at the die ( $Z = 0$ ). Then the discretized equations were written for each of the PDEs before moving on to the next grid point. This resulted in a banded Jacobian that greatly speeded up the calculations with DASSL.

The calculations started with 21 grid points, and these were increased until the computed results were unchanged within a minimum of four significant figures of accuracy. In investigating several options for the derivative routine DSS032, we found that the best compromise between promoting numerical accuracy and minimizing numerical oscillations resulted from using five-point biased upwind differences for  $\partial r/\partial \varsigma$ ,  $\partial h/\partial \varsigma$ ,  $\partial v/\partial \varsigma$ ,  $\partial \theta/\partial \varsigma$ , and  $\partial x/\partial \varsigma$ . The grid point allocation that met or exceeded the latter criterion was 105 points uniformly distributed from  $\varsigma = 0$  to 0.4, and 46 points uniformly distributed from  $\varsigma = 0.4$  to 1.0.

The startup condition used in the calculations consisted of first extruding and attaching the blown film tube to the nip rolls under conditions of uniform (with respect to axial position  $Z$ ) tube radius and film thickness. As DASSL functions better with smooth changes, the two stress constants  $B$  and  $F$  were increased from zero to finite values by using the switching functions

$$B(1 - \exp(-\tau^2/\tau_s^2)) \quad (26)$$

$$F(1 - \exp(-\tau^2/\tau_s^2)). \quad (27)$$

The switching function goes from zero to one as  $\tau$  increases from zero. DASSL was able to converge consistently, even with  $\tau_s$  values as low as 1.0.

The value of  $B$  is dependent on the pressure difference  $\Delta P$  across the film, as shown in the definitions of Table 2, and  $F$  is adjusted until the velocity  $v$  at  $Z = L$  reaches the desired take-up ratio ( $TUR$ ), which is the ratio of the velocity at  $Z = L$  to the velocity at the die

exit. The adjustment of  $F$  is accomplished by regula-falsi root finding (14).

## SIMULATIONS OF THE QUASI-CYLINDRICAL MODEL

Table 3 contains the operating conditions for the simulation and also gives the values for the physical parameters. The values in Table 3 gives good agreement between simulation and the higher blow-up ratio data of Liu (3–5) performed on low-density polyethylene (LDPE). The constitutive relation for this material was characterized by the extensive experiments of Liu (3–5), from which the property values in Table 3 are taken.

As simulations of Liu and co-workers for blown-film extrusion were at steady state, our steady-state results were compared first with the published results. To verify the accuracy of the steady-state results obtained by our finite difference code, the steady-state results were computed by two methods: 1) the transient finite difference code was run for sufficiently long time to reach steady-state, and 2) the ordinary differential equations obtained by setting the time derivatives in Eqs 1 to 5 to zero and algebraically decoupling the spatial derivatives were directly solved using DASSL. The transient finite difference code (method 1) was run for a long period of time with the grid points refined until its computed results agreed with those of the steady-state calculations (method 2). Excellent agreement between the two methods was achieved for  $\tau = 5000$  dimensionless time units and  $N_z = 151$  grid points distributed as described in the previous section.

### Steady-state Results

#### Comparison With Experiment

Figures 2a, 2b, and 2c show the computed bubble-tube radius, film velocity, and temperature profiles, respectively, corresponding to the parameter values

Table 3. Values of Constants Used in Simulations

$\lambda_a$	4.68 s
$b$	0.68
$C_3$	85,000 K <sup>2</sup>
$H_0$	0.095 cm
$k_{crys}$	2670 s <sup>-1</sup>
$H_0$	0.746 cm
$T_{air}$	331 K
$T_g$	118 K
$T_m$	414 K
$T_0$	463 K
$U_h$	50.27 W/m <sup>2</sup> -K
$U^*$	6284 kJ/kmol
$\alpha_1$	0.96 Pa-s
$\alpha_2$	13.5
$\beta_1$	4480 K
$\beta_2$	0.4
$X_f$	0.44
$\Delta H_{crys}$	293.2 kJ/kg
$\rho$	919 kg/m <sup>3</sup>
$\tau_s$	1.0

shown in Table 3,  $\Delta P = 291.1$  Pa,  $V_0 = 0.391$  cm/s,  $F = 0.2639$ . Also shown is the experimental data of Liu under the same conditions for a blow-up ratio equal to 2.71. The stress-thinning relaxation time  $\lambda_a$  was used as a fitting parameter, with a good fit obtained only with  $\lambda_a \neq 0$ . Inclusion of viscoelastic effects in the constitutive relation and the momentum equations did not improve the data fit, regardless of the value of  $\lambda_a$ .

*Differences in Quasi-cylindrical and Thin Shell Models*

To demonstrate the quantitative difference between the quasi-cylindrical (QC) and thin shell (TS) models at steady state, Fig. 3 plots the difference in bubble-tube radius between the two models,  $R_{TS} - R_{QC}$ , versus the axial position  $Z$  for  $\Delta P = 270$  Pa,  $V_0 = 0.366$  cm/s, a take-up ratio  $TUR = 2.988$ , and the parameters in Table 3. The corresponding plot for film thickness,  $H_{TS} - H_{QC}$ , is shown in Fig. 4. The difference between the predictions of the two models is most significant at higher inflation pressures, typical of experimental conditions. At the inflation pressure  $\Delta P = 270$  Pa, the longitudinal curvature terms (which are omitted in the quasi-cylindrical model) exert significant radial force on the bubble, so that the thin shell model gives a larger final bubble-tube radius and a thinner film. The larger the inflation pressure  $\Delta P$ , the larger the effect of the longitudinal curvature.

*Blow-up Ratio Versus Thickness Ratio*

Based on the results at a single inflation pressure and machine tension, it might be expected that the TS model would always yield a larger bubble radius than the QC model if the inflation pressure was the same. The relationships are much more complicated when comparing results of the two models when other quantities are fixed. Corresponding to the parameters in Table 3, blow-up ratio (BUR) versus thickness reduction ( $TR = H_0/H_L$ ) curves were generated for both the TS and QC models, assuming an inlet melt temperature of 463 K and inflation pressures of 270, 280, and 284 Pa. In generating the BUR versus TR curve, shown in Fig. 5, the inflation pressure was held constant, and the modified machine tension  $F$  was decreased from right to left along the lower branch of the curve and from left to right along the upper branch. Thus, the upper branch of the BUR vs. TR curve corresponds to lower values of the machine tension  $F$ .

The BUR vs. TR curves are a much stronger function of the inflation pressure for the TS model than the QC model. The differences between the models are largest for high blow-up ratios, typical of industrial operations. Compared to the QC model, the TS model tends to have a more limited value of the blow-up ratio but a higher degree of thinning. This is due to the tendency of the longitudinal curvature terms in the momentum equation to pull the bubble more strongly in the direction of the roller.

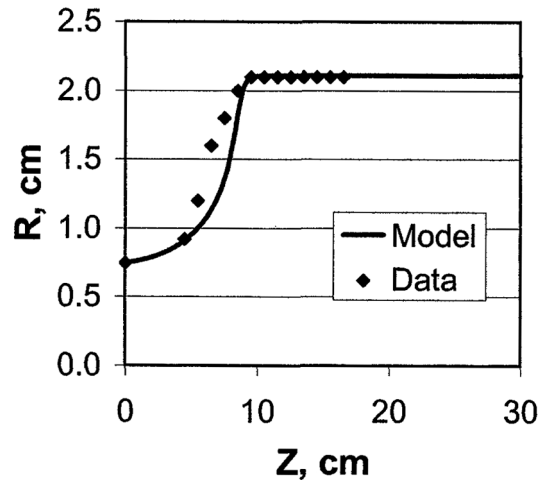


Fig. 2a. Bubble-tube radius: experimental and quasi-cylindrical model profiles, steady-state,  $\Delta P = 291.1$  Pa,  $V_0 = 0.391$  cm/s,  $F = 0.2639$ , Table 3 parametric values.

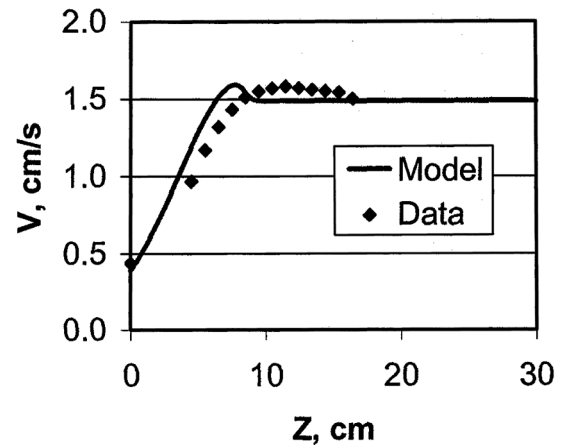


Fig. 2b. Film velocity: experimental and quasi-cylindrical model profiles, steady-state,  $\Delta P = 291.1$  Pa,  $V_0 = 0.391$  cm/s,  $F = 0.2639$ , Table 3 parametric values.

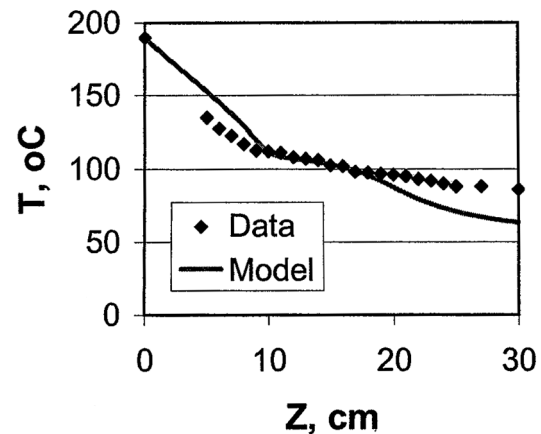


Fig. 2c. Film temperature: experimental and quasi-cylindrical model profiles, steady-state,  $\Delta P = 291.1$  Pa,  $V_0 = 0.391$  cm/s,  $F = 0.2639$ , Table 3 parametric values.

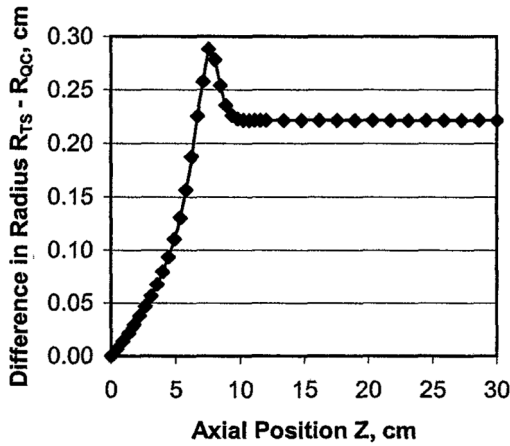


Fig. 3. Difference in bubble-tube radius between thin shell and quasi-cylindrical models: steady-state,  $\Delta P = 270$  Pa,  $V_0 = 0.366$  cm/s,  $TUR = 2.988$ , Table 3 parametric values.

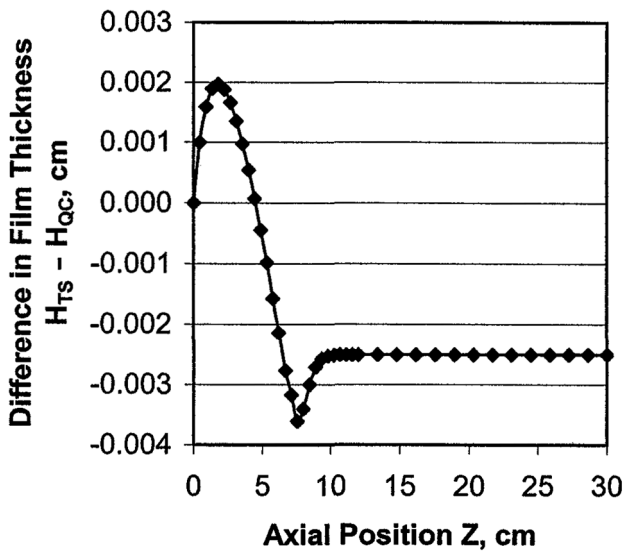


Fig. 4. Difference in film thickness between thin shell and quasi-cylindrical models: steady-state,  $\Delta P = 270$  Pa,  $V_0 = 0.366$  cm/s,  $TUR = 2.988$ , Table 3 parametric values.

Effect of Machine Tension  $F$

For  $V_0 = 0.366$  cm/s and conditions given in Table 3, the machine tension  $F$  was increased from 0 to determine the range of inflation pressures that yielded stable bubbles. Corresponding to each value of machine tension  $F$ , there is a lower and upper inflation pressure that allows physical solutions. Above the maximum inflation pressure, the radius increases without bound, mimicking a burst bubble. Below the minimum inflation pressure, the radius collapses to an infinitesimal quantity, mimicking a rapidly moving filament of vanishing diameter. As shown in Fig. 6, for the quasi-cylindrical model the minimum inflation pressure is zero for machine tensions ranging from  $F = 0$  to 0.1752, but

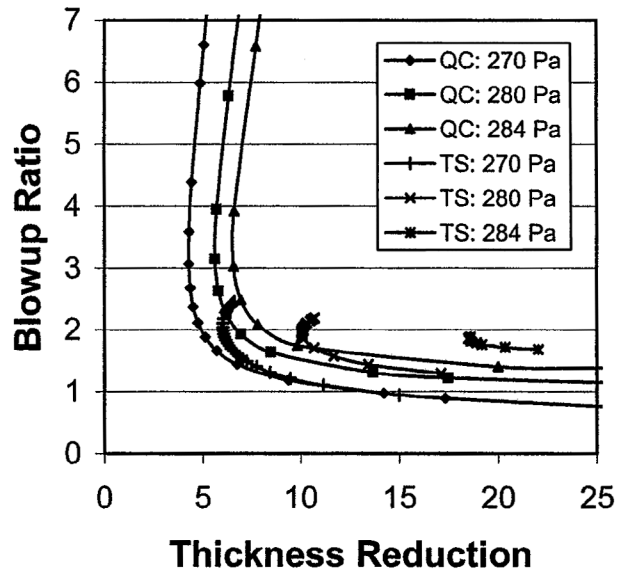


Fig. 5. Blow-up ratio versus thickness reduction: comparison of quasi-cylindrical and thin shell models at various inflation pressures,  $V_0 = 0.391$  cm/s, Table 3 parametric values.

rises sharply to equal the maximum inflation pressure at the machine tension  $F = 0.2990$ . At higher machine tensions, there is no solution. For low values of machine tension, the bubble is stable for a wider range of inflation pressures for the quasi-cylindrical model than for the thin shell model. On the other hand, a stable bubble can be maintained by the quasi-cylindrical model only for much lower machine tensions. The region of bubble stability, with respect to inflation pressure and

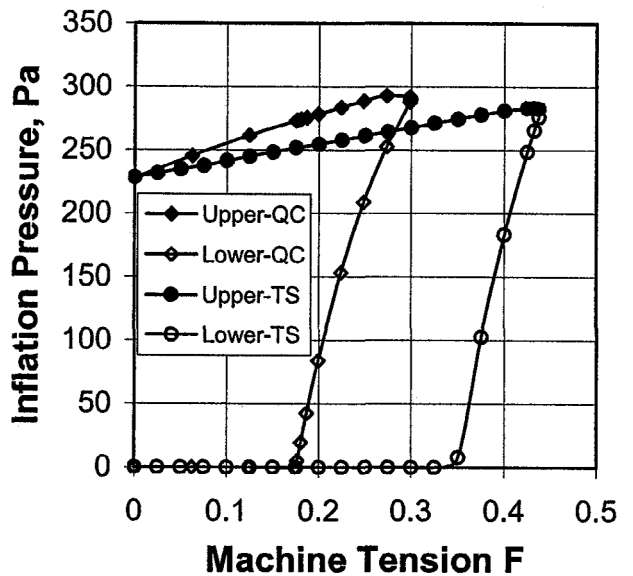


Fig. 6. Upper and lower inflation pressure bounds for different values of machine tension,  $V_0 = 0.366$  cm/s, Table 3 parametric values.

machine tension, is ~60% larger for the thin shell model than for the quasi-cylindrical model. This difference would have significant implications if the models were used to determine stable operating conditions for an industrial blown film extruder.

**Dynamic Behavior**

Here the dynamic behavior of the thin shell and quasi-cylindrical models are compared in terms of transient shifts between steady-state operating conditions, and in terms of the effect of oscillations in heat transfer characteristics and the inflation pressure. All calculations use the parameters given in Table 3 and  $V_0 = 0.366$  cm/s.

*Transient Shift Between Steady States*

The goal of these simulations is to determine how smoothly the blown film extrusion process can be shifted from one steady state to another. The initial inflation pressure and the machine tension are  $B = 0$  and  $F = 0$ , respectively, which corresponds to a take-up ratio  $TUR = 1$  and a flat bubble-tube radius and film thickness profile ( $r = 1$  and  $h = 1$  for  $\zeta = 0$  to 1). At time  $\tau = 0$ , the inflation pressure  $B$  and machine tension  $F$  are shifted to new values of 0.14128 (which corresponds to  $\Delta P = 270$  Pa) and 0.25035, respectively. These new values also correspond to a take-up ratio of 2.988. In the simulation, the mathematical functions used for the shift were

$$B_{new} = B_{old} + (B_{new} - B_{old})[1 - \exp(-\tau^2/\tau_{shift}^2)] \quad (28)$$

$$F_{new} = F_{old} + (F_{new} - F_{old})[1 - \exp(-\tau^2/\tau_{shift}^2)] \quad (29)$$

The film velocity can experience an overshoot resulting from the rapid propagation of disturbances by the momentum balance (2) in the axial direction. The extent of this behavior depends on the value of the shifting time  $\tau_{shift}$ . The longer the shifting time, the less the excursion of the velocity, and the smoother the transition. For  $\tau_{shift} = 30$ , which is roughly the travel time of the film from  $Z = 0$  to  $Z = L$ , the overshoot in the velocity is virtually eliminated. For  $\tau_{shift} < 30$ , the velocity profile overshoots its final steady-state value; the lower the value of  $\tau_{shift}$ , the greater the overshoot. The main concern from the perspective of process operation is that such a gyration in the film velocity can cause wrinkling of the sheet if the transition between steady states is not sufficiently gradual.

Figures 7 through 11 show how the dimensions and properties of the blown film develop over time when the inflation pressure  $\Delta P$  changes from 0 to 270 Pa and the machine tension  $F$  changes from 0 to 0.25035. The profiles in Figs. 7 to 9 develop smoothly with time, almost reaching the new steady state in a monotonic fashion within 81 dimensionless time units (~165 seconds or 4 times  $L/V_0$ ). In contrast, the temperature profiles in Fig. 10 at  $\tau = 21$  and 41 rise above the initial profile, and then decline to values below the initial profile. In

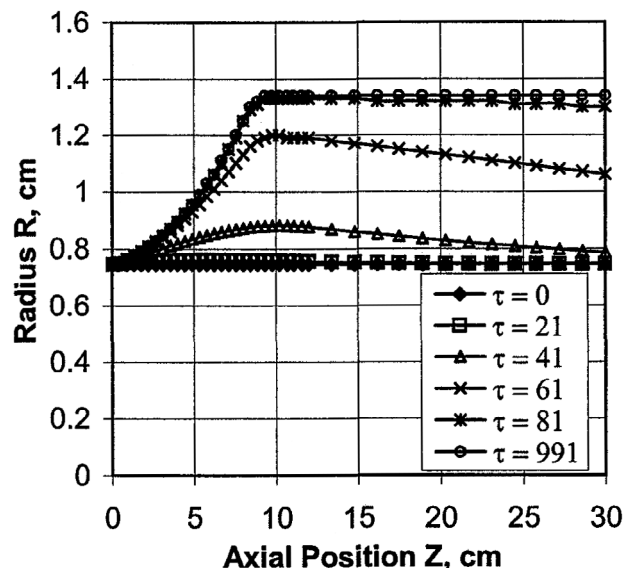


Fig. 7. Bubble-tube radius profiles after shift to new inflation pressure  $\Delta P$  and machine tension  $F$  ( $\tau_{shift} = 30$ ).

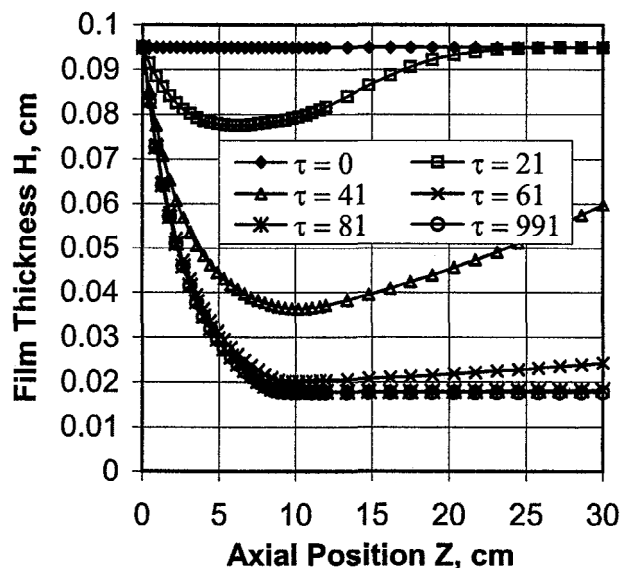


Fig. 8. Film thickness profiles after shift to new inflation pressure  $\Delta P$  and machine tension  $F$  ( $\tau_{shift} = 30$ ).

Fig. 11, the crystallinity profiles initially decrease before increasing to its final profile. This “inverse response” effect is much more pronounced for the crystallinity than for the temperature because of the sensitive dependence of the crystallization rate upon temperature. Behavior similar to that shown in Figs. 7 to 11 was observed for other values of the inflation pressure, machine tension, and extrusion temperature. The “inverse response” effect was also observed in dynamic simulations of the thin shell model (7).

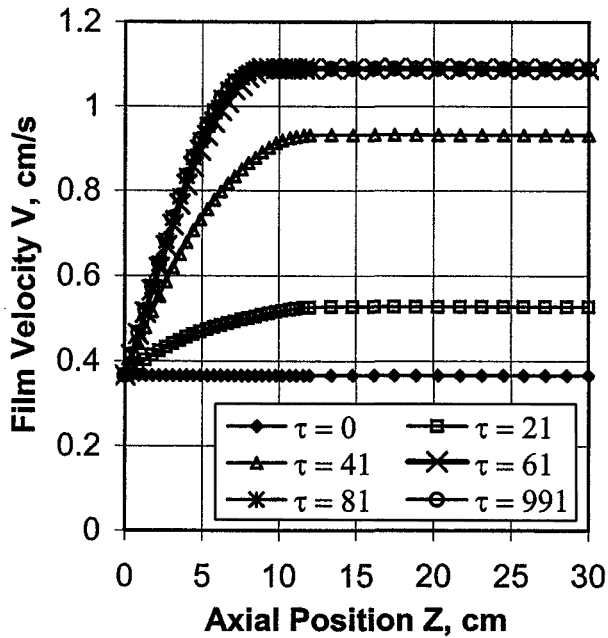


Fig. 9. Film velocity profiles after shift to new inflation pressure  $\Delta P$  and machine tension  $F$  ( $\tau_{\text{shift}} = 30$ ).

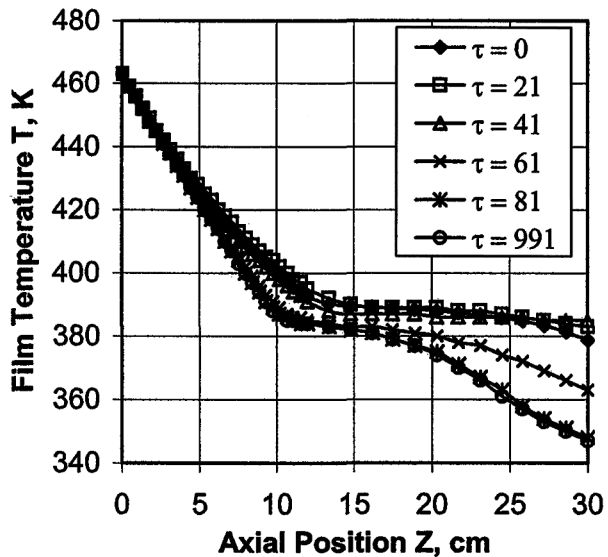


Fig. 10. Film temperature profiles after shift to new inflation pressure  $\Delta P$  and machine tension  $F$  ( $\tau_{\text{shift}} = 30$ ).

#### Oscillations in Operating Conditions

Heat transfer from film to cooling air. In most experimental and commercial blown film extruders, externally and internally flowing air cools the film tube as it leaves the die. Proper cooling is important to get an acceptable viscosity profile and to obtain proper crystallization. The rate of cooling affects the dimensions and strength of the film tube. The film to air heat transfer coefficient  $U_h$  depends on the physical properties of the air as well

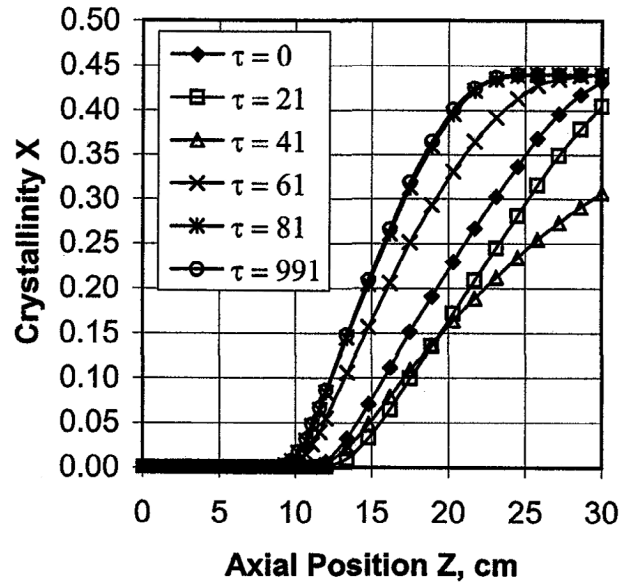


Fig. 11. Crystallinity profiles after shift to new inflation pressure  $\Delta P$  and machine tension  $F$  ( $\tau_{\text{shift}} = 30$ ).

as the pattern of flow in the boundary layer next to the film. In the calculations that follow, the inflation pressure  $\Delta P = 265$  Pa, and the time-averaged take-up ratio  $TUR = 2.988$ .

Variations in the final bubble tube radius  $r_L$  (that is, the dimensionless radius at the top of the freeze zone  $Z = L$ ) were computed for oscillations in the heat transfer coefficient with frequency  $\nu$  and amplitude of 4% or 10% of the steady value (taken as  $50 \text{ W/m}^2\text{-K}$ ). It was observed that the frequency of variation of the bubble-tube radius  $r_L$  follows the frequency in the oscillation of the heat transfer coefficient  $U_h$  extremely closely and is practically equal to  $\nu$ . In Fig. 12, the maximum and minimum values of the final bubble-tube radius  $r_L$  are plotted as  $r_L - r_{L,ss}$ , where the steady-state bubble-tube radius  $r_{L,ss}$  is the value of the bubble-tube radius  $r_L$  for no oscillation in the heat transfer coefficient  $U_h$ . The upper and lower values of the maximum deviation ( $r_L - r_{L,ss}$ ) are not symmetric about zero. This can be attributed to the nonlinear effect of the temperature on the viscosity, which, in turn, has a profound effect of the deformation of the bubble. As expected for physical systems, the maximum deviation approaches zero for high enough frequencies. However, this decline is not monotonic, as there are local minima and maxima in the plots at frequency  $\nu = 0.1379, 0.1818, 0.2538, 0.3077, 0.3704, 0.4211, \text{ and } 0.5000$ .

The mean maximum deviation of the bubble-tube radius  $r_L$  is defined as the maximum bubble-tube radius  $r_L$  minus its minimum value divided by two (see Fig. 13). The local minima and maxima are more clearly seen in Fig. 13. The maximum value of the bubble-tube radius  $r_L$  at low frequencies is fairly sensitive to the variation in the heat transfer coefficient  $U_h$ . Oscillations of amplitudes of  $\pm 4\%$  and  $10\%$  in the heat transfer coefficient  $U_h$  result in mean maximum variations in the

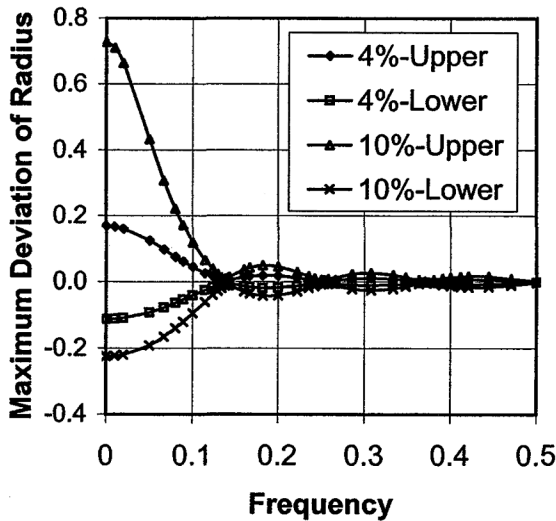


Fig. 12. Maximum deviation of the final bubble-tube radius  $r_L$  as a function of frequency of oscillation of the heat transfer coefficient  $U_h$ .

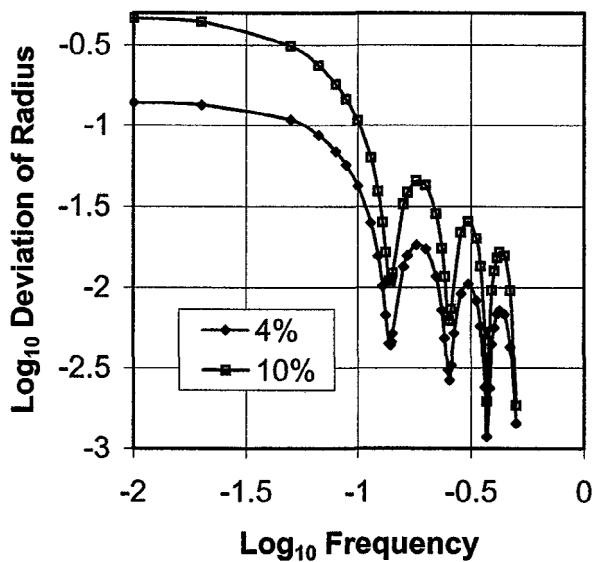


Fig. 13. Mean maximum variation in the final bubble-tube radius  $r_L$  as a function of frequency of oscillation of the heat transfer coefficient  $U_h$ .

bubble-tube radius  $r_L$  of 8.4% and 28.4%, respectively, at low frequencies.

There are profound qualitative (as well as quantitative) differences between Figs. 12 and 13 and the corresponding plots for the thin shell model (7), which exhibit no minima or maxima at intermediate frequencies. This difference is significant from a design and control point of view. The quasi-cylindrical model predicts that either an increase or decrease in the frequency of oscillations in the heat transfer characteristics may result in a reduced effect on the bubble shape. The thin shell model

predicts that the bubble-tube radius is always more sensitive to low-frequency disturbances in heat transfer characteristics than high-frequency disturbances.

**Inflation air pressure.** Next, the effect of oscillations of the inflation pressure on the operation of blown film extrusion was determined. For the conditions in Table 3 and a time-averaged take-up ratio  $TUR = 2.988$ , amplitudes of variation of inflation pressure of 2% and 6% around 265 Pa were examined. Above an amplitude of 9%, the bubble grows without bound, achieving conditions for rupture. For 2% and 6% variations of inflation pressure, Fig. 14 shows the maximum and minimum deviations in the final bubble-tube radius  $r_L$  as a function of frequency  $\nu$ . The deviations are not symmetrical about zero, but, unlike those corresponding to oscillations in heat transfer coefficients, they decrease monotonically as frequency increases. The relationship between the inflation pressure and bubble-tube radius is nonlinear for 6% variations in inflation pressure.

The mean maximum deviation in the bubble-tube radius  $r_L$  (maximum value of  $r_L$  minus minimum value of  $r_L$  divided by two) is plotted in Fig. 15. This log-log plot shows minor kinks in the plots for frequencies above 0.1. This behavior of the quasi-cylindrical model is qualitatively (as well as quantitatively) different from the thin shell model (7), which does not have a monotonic decline in mean maximum deviation of the bubble-tube radius  $r_L$  with frequency  $\nu$ . For the thin shell model, the mean maximum deviation in the bubble-tube radius has a distinct minimum at  $\nu = 0.12$ , which climbs back to a maximum at  $\nu = 0.15$ , and then decreases for higher frequencies.

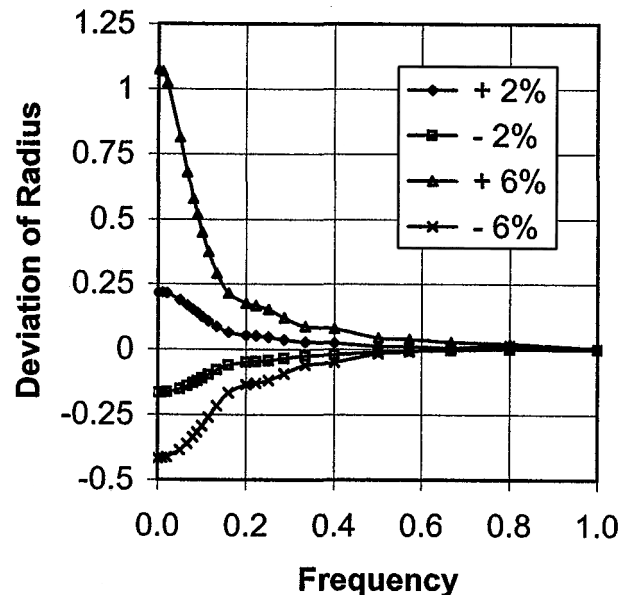


Fig. 14. Maximum deviation of the final bubble-tube radius  $r_L$  as a function of the frequency of oscillation of the inflation pressure.

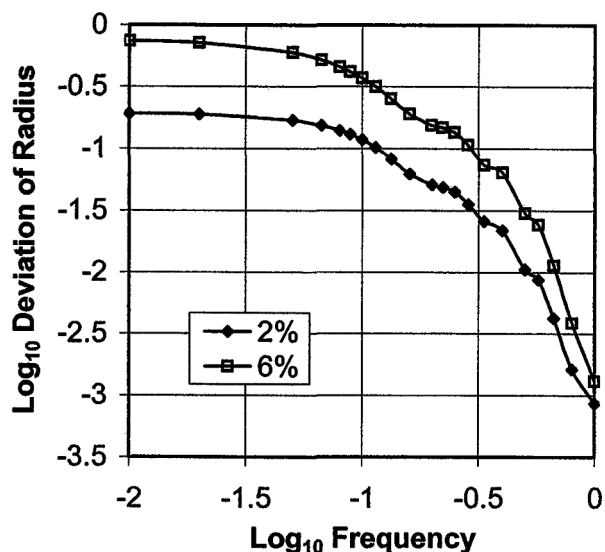


Fig. 15. Mean maximum amplitude of deviation of the final bubble-tube radius  $r_1$ , as a function of the frequency of oscillation of the inflation pressure.

### CONCLUSIONS

Some of the steady-state predictions of the quasi-cylindrical and thin shell models are in qualitative agreement. In particular, the film tube radius is seen to increase with inflation pressure over a wide range of conditions for both models. There are, however, some noticeable quantitative differences between the two models that increase with inflation pressure. The most significant observed difference in steady-state behavior was that the region of bubble stability is much larger for the thin shell model (see Fig. 6). Such differences can significantly affect the design and expected operation of a blown film extruder. In addition, the quasi-cylindrical model predicts that the blown film extruder can operate under much higher values of the blow-up ratio for fixed values of the inflation pressure compared to the thin shell model. Finally, the two models exhibit different responses to oscillations to process variables

such as the heat transfer characteristics and inflation pressure. The differences are large enough to suggest that the thin shell model should be used in dynamic studies, whether the goal of the studies is improved process understanding, the study of film instabilities, or the design of control systems or improved blown film extrusion processes.

### ACKNOWLEDGMENT

Dr. Mitsuko Fujiwara is acknowledged for aid in manuscript preparation.

### REFERENCES

1. J. R. A. Pearson and C. J. S. Petrie, *J. Fluid Mech.*, **40**, 1 (1970).
2. J. R. A. Pearson and C. J. S. Petrie, *J. Fluid Mech.*, **42**, 609 (1970).
3. C.-C. Liu, D. C. Bogue, and J. E. Spruiell, *Intern. Polym. Process.*, **10**, 230 (1995).
4. C.-C. Liu, *Studies of Mathematical Modelling and Experimental On-Line Measurement Techniques for the Tubular Film Blowing Process*, M.S. thesis, Dept. of Materials Science and Engineering, University of Tennessee, Knoxville (1991).
5. C.-C. Liu, *On-Line Experimental Study and Theoretical Modelling of Tubular Film Blowing*, Ph.D. thesis, Dept. of Materials Science and Engineering, University of Tennessee, Knoxville (1994).
6. A. K. Doufas and A. J. McHugh, *J. Rheology*, **45**, 1085 (2001).
7. J. C. Pirkle Jr., and R. D. Braatz, *Polym. Eng. & Sci.*, **43**, 398 (2003).
8. C.-C. Liu, D. C. Bogue, and J. E. Spruiell, *Intern. Polym. Process.*, **10**, 226 (1995).
9. B. K. Ashok and G. A. Campbell, *Intern. Polym. Process.*, **7**, 240 (1992).
10. Y. L. Yeow, *J. Fluid Mech.*, **75**, 577 (1976).
11. W. E. Schiesser, *The Numerical Method of Lines Integration of Partial Differential Equations*, Academic Press, San Diego (1991).
12. C. A. Silebi and W. E. Schiesser, *Dynamic Modeling of Transport Process Systems*, p. 409, Academic Press, San Diego (1992).
13. L. R. Petzold, "A description of DASSL: a differential/algebraic system solver," in *Scientific Computing*, pp. 65–68, R. S. Stepleman, ed., IMACS, North-Holland (1983).
14. F. Scheid, *Numerical Analysis*, p. 311, McGraw-Hill, New York (1968).